



HAL
open science

Potential for calcination of a palygorskite-bearing argillaceous carbonate

Victor Poussardin, Michael Paris, Arezki Tagnit-Hamou, Dimitri Deneele

► **To cite this version:**

Victor Poussardin, Michael Paris, Arezki Tagnit-Hamou, Dimitri Deneele. Potential for calcination of a palygorskite-bearing argillaceous carbonate. *Applied Clay Science*, 2020, 198, pp.105846. 10.1016/j.clay.2020.105846 . hal-03109843

HAL Id: hal-03109843

<https://hal.science/hal-03109843>

Submitted on 23 Mar 2021

HAL is a multi-disciplinary open access archive for the deposit and dissemination of scientific research documents, whether they are published or not. The documents may come from teaching and research institutions in France or abroad, or from public or private research centers.

L'archive ouverte pluridisciplinaire **HAL**, est destinée au dépôt et à la diffusion de documents scientifiques de niveau recherche, publiés ou non, émanant des établissements d'enseignement et de recherche français ou étrangers, des laboratoires publics ou privés.

1 **Potential for calcination of a palygorskite-bearing** 2 **argillaceous carbonate**

3

4 Victor Poussardin^{1,2}, Michael Paris¹, Arezki Tagnit-Hamou³, Dimitri Deneele^{1,2*}

5 ¹*GERS-LGIE, Univ Gustave Eiffel, IFSTTAR, F-44344 Bouguenais, France*

6 ²*Université de Nantes, CNRS, Institut des Matériaux Jean Rouxel, IMN, F-44000 Nantes,*
7 *France*

8 ³*Université de Sherbrooke, Sherbrooke, QC, Canada*

9 *corresponding author: dimitri.deneele@univ-eiffel.fr

10 **Highlights**

- 11 • The thermal reactivity of an argillaceous-carbonate sample is studied.
- 12 • A calcination temperature of 800°C allows a dehydroxylation of the clayey phases
- 13 • Evolution of the sample is quantified as a function of the calcination temperature
- 14 • The calcination leads to the formation of belite (C2S) from 700°C
- 15 • Calcined-Palygorskite-rich carbonate represents an opportunity for use as SCM

16 **Abstract**

17 The intensive use of cement as a building material causes significant pollution. The majority of
18 CO₂ emissions come from the manufacturing process and not from the product itself. Indeed,
19 the decarbonation of limestone and the use of fuels during clinkerisation are very polluting. One
20 of the main solutions to reduce the environmental footprint of the cement industry is the use of
21 Supplementary Cementitious Materials (SCMs) in substitution of clinker. Among them are
22 glass powders, fly ashes, blast-furnace slags or calcined clays. This article focuses on the
23 thermal reactivity of an argillaceous-carbonate sample containing palygorskite, smectite and
24 dolomite. The sample was calcined at different temperatures and investigated using Solid State

25 Nuclear Magnetic Resonance (NMR), X-ray diffraction (XRD), and Scanning Electron
26 Microscope (SEM). The increase in calcination temperature leads to an amorphisation of the
27 clay fraction of the sample, resulting in a change in the coordination of the octahedral
28 aluminium atoms. The progressive transformation of 6-fold aluminium atoms to 5-fold and 4-
29 fold was quantified as a function of the calcination temperature. Furthermore, calcium issued
30 from the decarbonation of dolomite reacts with silicon from the amorphisation of clay phases
31 to form poorly-crystallized belite (C₂S). This dual system (pozzolanic and hydraulic) makes
32 this sample a promising candidate as SCM in blended cements. The multi-technique analysis
33 applied in this study allows to highlight a direct correlation between the calcination temperature
34 and the induced structural modification.

35 **Keywords:** Palygorskite, calcination, belite, ²⁹Si NMR, ²⁷Al NMR, Rietveld refinement

36 **1. INTRODUCTION**

37 It is estimated that cement production is responsible for 5-8% of total anthropogenic CO₂
38 emissions (Huntzinger and Eatmon, 2009). In an international context promoting the reduction
39 of CO₂ emissions, the cement industry appears to be a bad pupil. The fault resides in
40 clinkerization, the process by which clinker, the basic product of Portland cement, is obtained.
41 Both the use of mostly fossil fuels and the decarbonation of limestone during the process are
42 contributing to the majority of CO₂ emissions (Cancio Díaz et al., 2017). Faced to this alarming
43 observation, the cement industries are now turning to the research and development of new
44 supplementary cementitious materials (SCMs) that can partially replace clinker in order to
45 drastically reduce CO₂ release and the environmental cost of Ordinary Portland Cement (OPC)
46 manufacture. These innovations include the use of additives from industry (blast furnace slags
47 (Escalante et al., 2001), fly ash from power plants (Sakai et al., 2005)), natural additives (clays
48 (Horpibulsuk et al., 2012)) and artificial additives (calcined clays). The Limestone Calcined

49 Clay Cement (LC³) project (Scrivener et al., 2018) is a good example of the use of calcined clay
50 as SCM. The substitution of 50% of the clinker with 20% limestone and 30% metakaolin
51 reduces the environmental footprint of OPC by 20-23% while maintaining the delivery of
52 cement with satisfactory mechanical properties (Cancio Díaz et al., 2017). Numerous studies
53 have shown that kaolinite dehydroxylation during calcination leads to the production of very
54 reactive SCM metakaolin, (El-Diadamony et al., 2018). In addition, the available kaolinite
55 resources with potential for calcination are relatively well distributed on earth (Prasad et al.,
56 1991), making it possible to envisage large-scale use. In this context, the majority of scientific
57 research has been focused on the calcination of kaolins, sometimes neglecting the study of less
58 common clays. However, understanding the reactivity of other types of natural materials
59 containing clays is essential to envisage the valorisation of secondary clayey resources, refine
60 our knowledge and propose new innovative solutions to reduce the CO₂ emissions of the OPC
61 production. Natural samples rich in palygorskite are one of these interesting materials to test as
62 SCM.

63 Palygorskite is a clayey mineral consisting of TOT-type ribbons. Several studies have shown
64 that TOT clays, mainly montmorillonites and illites, are not ideal as SCM (Hollanders et al.,
65 2016; Danner et al., 2018), mainly due to the resistance of their structure to heat treatment. The
66 particularity of palygorskite structure compared to montmorillonite and illite is that the
67 tetrahedra are reversed when passing from one ribbon to the other. This alternation creates
68 channels that are filled with zeolitic water, and confers to palygorskite a three-dimensional
69 structure (Galan, 1996). These channels provide to the palygorskite an important internal
70 surface and hence large specific surface area, high sorption capacity, and microporosity. Its
71 general formula is (Mg,Al)₂Si₄O₁₀(OH).4H₂O but isomorphic substitutions are possible, in
72 particular of silicon by aluminium in tetrahedral sheets (Blanco et al., 1989).

73 As specified above, the latest studies on blended cement deal with the addition of metakaolin
74 and calcium carbonate to the blended cement. Indeed, limestone will improve the hydration
75 reactions of the different phases of the clinker by acting as a nucleation surface for the hydrates
76 produced. It will also react with the active alumina (from calcined clay) to form
77 carboaluminates. These carboaluminates will stabilize the Ettringite that forms at the early
78 stages of hydration and prevent its transformation into monosulphate. The Ettringite thus
79 stabilised can fill more space than in the monosulphate form, helping to improve the mechanical
80 properties (Bonavetti et al., 2001; Ipavec et al., 2011).

81 However, only few studies describe the addition of a calcined natural argillaceous-carbonate
82 (Danner et al., 2018; Soltani et al., 2018). Then, we decided to progress by studying the potential
83 for calcination of an argillaceous-carbonate containing palygorskite as a potential SCM. The
84 aim is to describe the physico-chemistry of the raw material, to identify and understand the
85 physicochemical modifications induced by the calcination, and to define its optimum
86 calcination temperature.

87 **2. MATERIALS AND EXPERIMENTAL METHODS**

88 **2.1. Material**

89 The studied sample is a mining waste collected from a phosphate sedimentary deposit of a late
90 Cretace-Eocene age. The series includes carbonates, marl, silex and clayey layers that are
91 inserted between phosphate-rich layers, not exploited and considered as waste or a secondary
92 resource to valorise. Sample was received in the form of loose blocks and was crushed and
93 homogenized.

94 **2.2. Calcination**

95 The raw sample was calcined in alumina crucibles (about 3g of sample per crucible) using a
96 laboratory furnace without atmosphere control. The furnace used was a silicon carbide

97 laboratory chamber with a maximum operating temperature of 1500°C. The sample was heated
98 from 20°C up to 600, 700, 800 and 900°C with a heating rate of 300°C/h and a maximum
99 temperature time of 1h. The cooling rate was not controlled (inertia of the furnace door closed)
100 and the sample was collected after cooled down to room temperature (20°C). The choice of this
101 calcination protocol was made in accordance with the existing bibliography (Garg and Skibsted,
102 2014, 2016; Danner et al., 2018; Krishnan et al., 2019; Trümer et al., 2019).

103 **2.3. X-ray diffraction analysis**

104 X-ray diffraction analysis were performed using a Bruker D5000 diffractometer with a Bragg-
105 Brentano geometry. The source consists of a Cu anode tube (40 kV / 40 mA) that emits Cu K α 1
106 X-ray radiation (8 keV) of a wavelength $\lambda = 1.5418 \text{ \AA}$. The diffractograms of disoriented
107 powders were recorded between 3° and 90° 2 θ with a step size of 0.026° 2 θ and a measurement
108 time of 17s per step.

109 The diffractograms used for Rietveld quantification were acquired on a Bruker D8
110 diffractometer with a Bragg-Brentano geometry, using Cu anode tube, with Ni filter and without
111 monochromator. The diffractograms were acquired between 4° and 90° 2 θ with a step size of
112 0.018° 2 θ and a measurement time of 6s per step. The quantification of the crystalline phases
113 was made by Rietveld refinement using the open source Rietveld refinement program BGMN
114 with Profex 4.0 interface (Doebelin and Kleeberg, 2015), the amorphous phase was quantified
115 by using corundum (alpha-phase, 99.95% min) as an internal standard (see supporting
116 informations).

117 **2.4. Nuclear magnetic resonance**

118 The ²⁷Al NMR MAS spectra were acquired using a 2.5 mm MAS probe on a Bruker Avance
119 III 500 MHz spectrometer. A $\pi/13$ excitation pulse length was used for a radio frequency field
120 of 11 kHz. The MAS frequency was 30 kHz. The repetition time was 1s.

121 The MAS ^{29}Si spectra were acquired using a 7 mm MAS probe on a Bruker NEO 300 MHz
 122 spectrometer. The rotor rotation speed was 5 kHz and the pulse length was $\pi/2$. Different
 123 repetition times between scans were tested to ensure quantitative results and the choice was
 124 made to use a time of 10s. It is important to note that the repetition time of 10s chosen is too
 125 short to obtain a quantitative signal from the Quartz. Indeed, due to its high crystallinity, a
 126 longer repetition time would be mandatory. However, in the present study, Quartz is unreactive
 127 and shorter repetition time can be used to save spectrometer time.

128 ^1H decoupling was performed during the acquisition on all spectra. ^{27}Al and ^{29}Si spectra are
 129 reference against an aqueous solution of $\text{Al}(\text{NO}_3)_3$ and TMS (Tetramethylsilane), respectively.
 130 Finally, spectral decompositions were realized using the dmfit software (Massiot et al., 2002).

131 **2.5. Scanning electron microscopy**

132 The raw sample as well as changes induced by calcination were examined by scanning electron
 133 microscopy (SEM) using a Hitachi SU5000 microscope. The samples (raw fragment, raw
 134 powder, calcined powder) were subjected to a silver coating before observations.

135 **3. CHARACTERIZATION OF THE RAW MATERIAL**

136 A chemical analysis of the raw sample was carried out by X-Ray Fluorescence (XRF), the
 137 proportions of oxides (expressed in weight %) are presented in Table 1.

138 Table 1: Chemical analysis of the raw argillaceous-carbonate

Oxide	FeO	CaO	SiO ₂	Al ₂ O ₃	K ₂ O	TiO ₂	Na ₂ O	V ₂ O ₅	P ₂ O ₅	MgO	LOI (1000°C)
wt. %	1.99	19.83	33.3	8.94	1.24	0.34	0.32	0.16	1.49	9.91	35.0

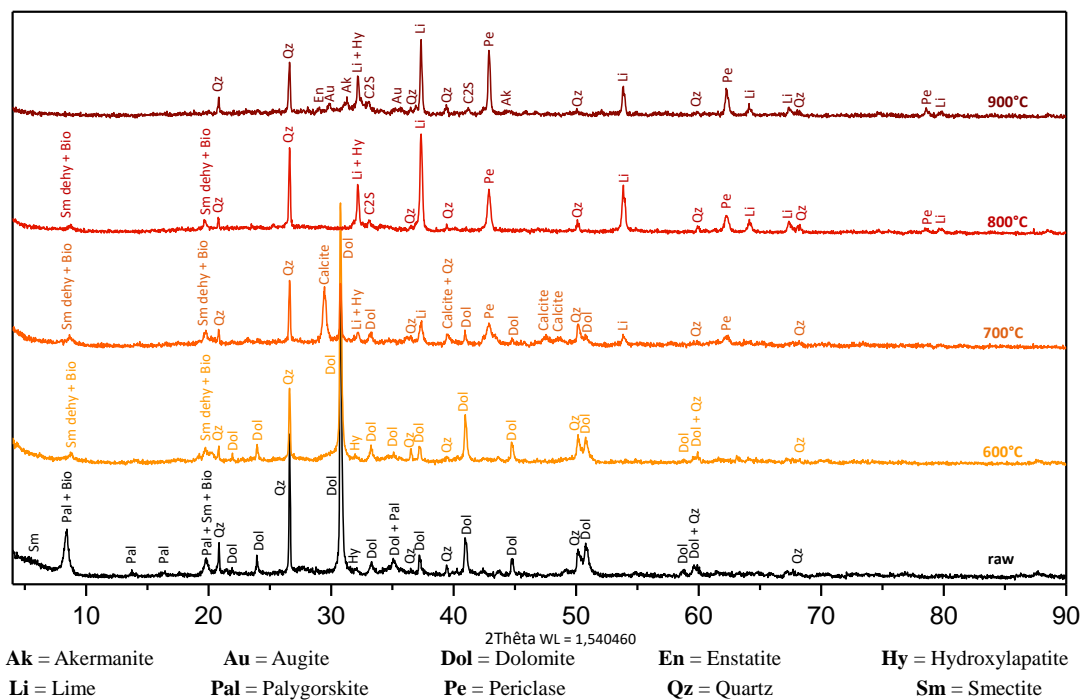
139

140 The oxides present in the highest quantity are SiO₂ (33.3 wt.%), CaO (19.83 wt.%), MgO (9.91
141 wt.%) and Al₂O₃ (8.94 wt.%). There is also a significant amount of FeO (1.99 wt.%), K₂O (1.24
142 wt.%) and P₂O₅ (1.49 wt.%).

143 Figure 1 displays the diffractograms of the raw argillaceous-carbonate samples. The
144 characteristic peaks of palygorskite (W.F.Bradley, 1940) ([110] 2θ=8.43°, [200] 2θ=13.73°,
145 [130] 2θ =16.26°, [040] 2θ=19.92) are observed. There is also a wide peak at around 2θ=6.2°
146 which is characteristic of the [001] peak of Ca-Smectite (Bala et al., 2000). The width of this
147 peak reflects the low crystallinity of this phase. palygorskite and Biotite, on the other hand,
148 seem to be better crystallized because their peaks are much thinner. The other main crystalline
149 phases composing this sample are dolomite, quartz, botite and hydroxylapatite. Table 2
150 presents the results of the Rietveld refinement of the raw material (details in Supporting
151 Information).

152 The sample is mainly composed of dolomite (Dol = 53 wt.%) associated with palygorskite (Pal
153 = 17.45 wt.%), Ca-smectite (Sm = 15.58 wt.%), quartz (Qz = 8.00 wt.%), hydroxylapatite (Hy
154 = 3.00 wt.%) and biotite (Bio = 2.41 wt.%). The addition of corundum as an internal standard
155 did not reveal the presence of amorphous phases. Therefore, Ca-smectite, palygorskite and
156 biotite are the only sources of aluminium. Ca-smectite, palygorskite, biotite and quartz are the
157 only sources of silicon in the material.

158



159

160 Figure 1 : Evolution of the X-ray diffractograms of the samples as a function of the
 161 calcination temperature

162 Table 2: Wt.% of the crystalline phases of the raw and 800°C argillaceous-carbonate samples.
 163 dolomite (Dol), biotite (Bio), lime (Li), periclase (Pe), palygorskite (Pal), Ca-smectite (Sm),
 164 Ca-smectite dehydrated (Sm dehy), quartz (Qz), hydroxylapatite (Hy), hematite (He), belite
 165 (C₂S), Am (Amorphous)

Raw	Phase	Dol			Pal	Sm	Qz	Hy	Bio		
	wt. %		53.58 (+/- 0.48)			17.45 (+/- 0.35)	15.58 (+/- 0.54)	8.00 (+/- 0.24)	3.00 (+/- 0.14)	2.41 (+/- 0.22)	
800°C	Phase	Li	Pe	He	Pal	Sm dehy	Qz	Hy	Bio	C2S	Am
	wt. %	19.41 (+/- 0.43)	17.11 (+/-0.37)	1.45 (+/- 0.10)	0.00	13.48 (+/- 0.48)	11.19 (+/- 0.27)	4.07 (+/- 0.17)	1.00 (+/- 0.19)	4.45 (+/- 0.20)	27.90 (+/- 1.60)

166

167

168

169

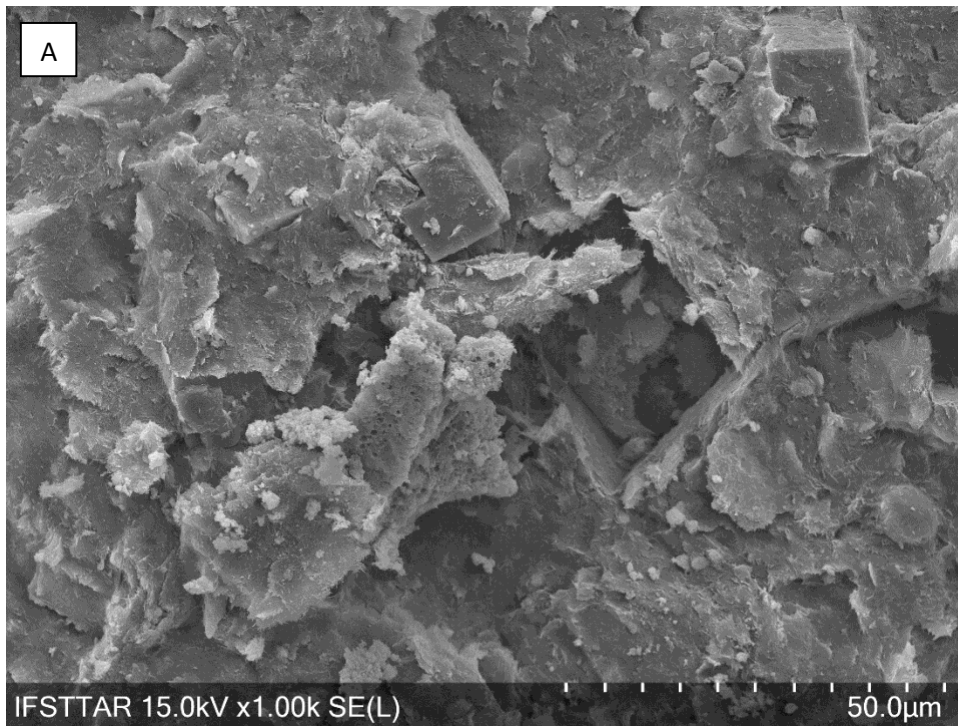
170

171

172

173

174



175

176

177

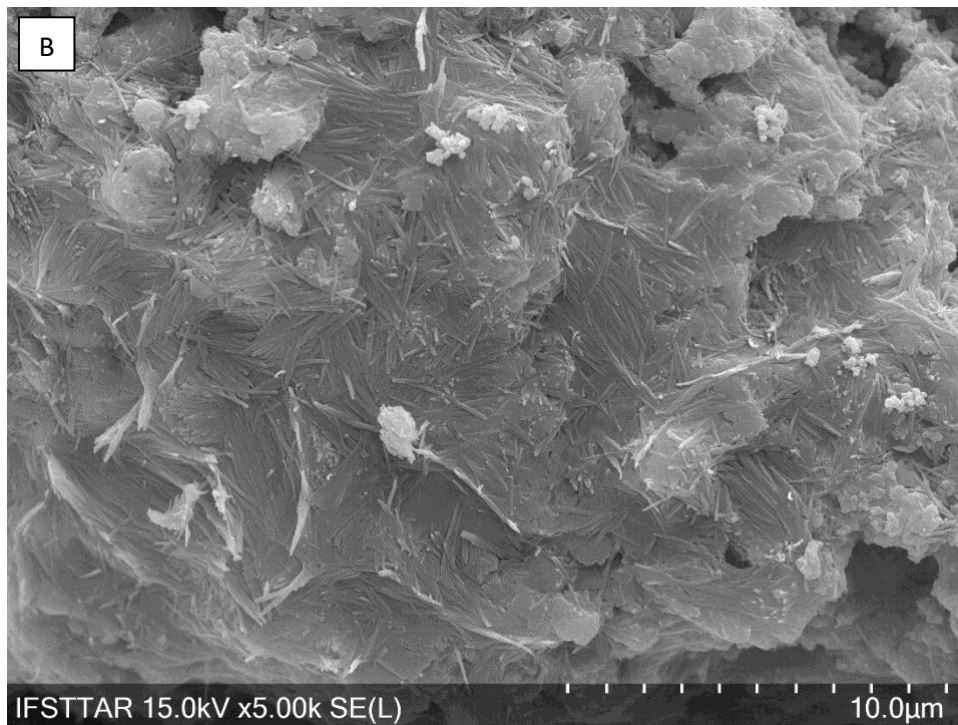
178

179

180

181

182



183

Figure 2: Scanning Electron Microscope images of the raw argillaceous-carbonate

184

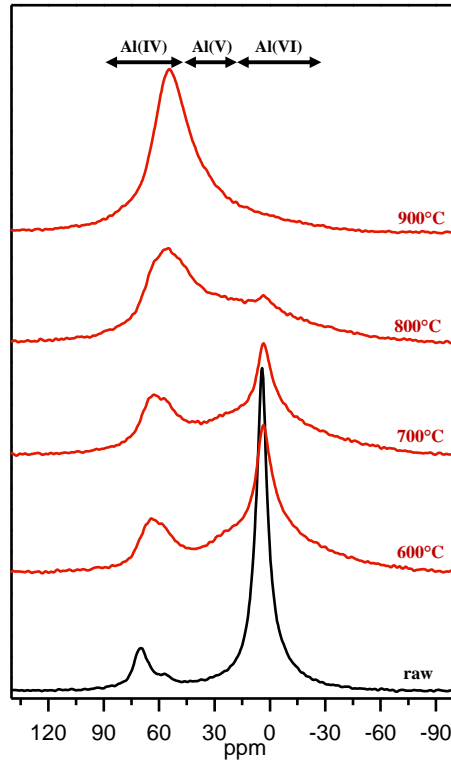
Figure 2 displays two SEM images (A and B) of a fragment of the raw argillaceous-carbonate

185

sample. Figure 2A shows the global morphology of the raw sample. dolomite rhombohedra are

186 clearly visible as well as the presence of a coating covering the entire sample. Figure 2B
187 displays another image of the surface of the sample at a higher magnification. The layer
188 covering the sample consists of a veil and very fine needles which are respectively characteristic
189 of smectite and palygorskite (Boudriche et al., 2011). It therefore appears that palygorskite and
190 smectite acts as a binder between the minerals in the sample and is present throughout the entire
191 sample. This latter information completes the analysis made by XRD. Despite its average mass
192 proportion (about 17 wt.%), the palygorskite is homogeneously distributed throughout the
193 entire sample and is in contact with all phases.

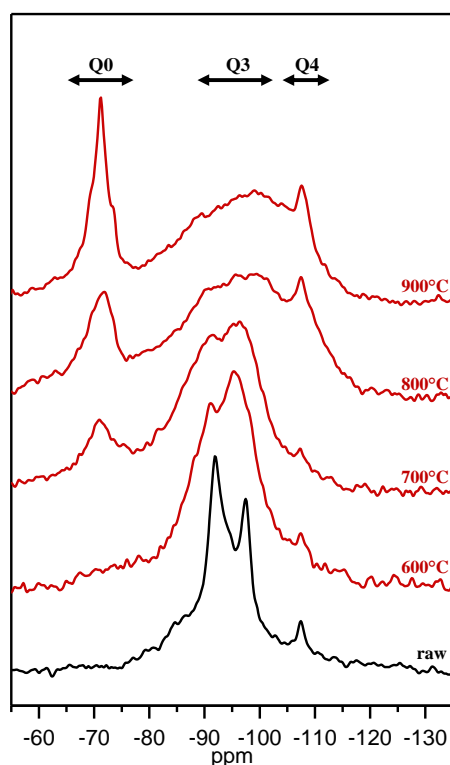
194 The ^{27}Al MAS NMR spectrum of the raw argillaceous-carbonate sample is shown in Figure 3.
195 It exhibits two main resonances at 3 and 70 ppm. The first intense resonance (3 ppm)
196 corresponds to hexacoordinated aluminium (Maia et al., 2014) and can be associated with
197 aluminium present in the palygorskite, Ca-smectite and biotite octahedra. The second resonance
198 at 70 ppm corresponds to tetraordinated aluminium (Maia et al., 2014) and can be associated
199 with substitution of silicon atoms by aluminium atoms in the Ca-smectite and/or palygorskite
200 tetrahedra (Sanz and Serratosa, 1984), and to a lesser extent to aluminium present within the
201 biotite tetrahedral sheets. There is also the presence of weak resonance at approximately 57
202 ppm which can be associated with $\text{AlO}_4 \text{q}^4(4\text{Si})$ (Muller et al., 1986). Aluminium present in the
203 $\text{q}^4(4\text{Si})$ configuration seems to be associated with a phase in very low quantity and/or composed
204 of very small crystallites since the latter is not detectable by XRD.



205

206 Figure 3: Evolution of the ^{27}Al MAS NMR spectra of the argillaceous-carbonate as function
 207 of the calcination temperature.

208 Figure 4 displays the ^{29}Si MAS NMR spectrum of the raw sample. The two main resonances at
 209 -92 and -98 ppm are attributed to palygorskite. They correspond to silicon in Q3 configuration
 210 at the center and at the edges of the ribbons of tetrahedra, respectively (Barron et al., 1985).
 211 The high intensity of resonances characteristic of palygorskite demonstrates its good
 212 crystallinity. In addition, Ca-smectite and biotite revealed by XRD analysis also contribute to
 213 the total ^{29}Si NMR signal. Indeed Q3 of Ca-smectite exhibit resonance at -93 ppm (Brown et
 214 al., 1987) and Q2(1Al) of biotite resonates at -86 ppm (Mackenzie et al., 1987).



215

216 Figure 4: Evolution of the ^{29}Si MAS NMR spectra of the argillaceous-carbonate as a function
 217 of the calcination temperature.

218 The resonance observed at -108 ppm corresponds to the quartz in the sample (Lippmaa et al.,
 219 1980). The low resonance intensity at -93 ppm characteristic of smectite is explained by its very
 220 low crystallinity. Indeed, the existence of a local environment distribution for silicon atoms
 221 results in a broadening of the resonance, which is consistent with the observation made by XRD
 222 which suggests that Ca-smectite is very poorly crystallized.

223 4. EFFECTS OF CALCINATION

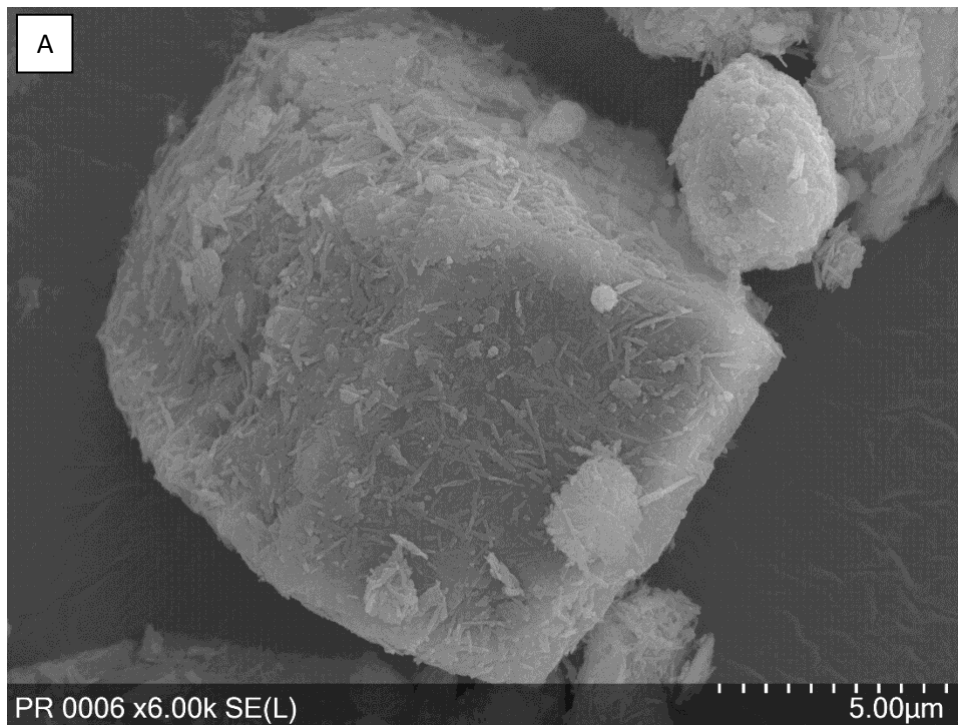
224 Figure 1 displays the evolution of the X-ray diffractograms of the samples as a function of the
 225 calcination temperature. Above 600°C, there is the disappearance of the peaks of palygorskite.
 226 This indicates a loss of crystallinity of the palygorskite phase in the sample. The shift of the

227 [001] characteristic peak of the Ca-smectite from about $2\theta = 6.2^\circ$ to $2\theta = 8.75^\circ$ is caused by the
228 decrease of the d001 value due to the removal of the water from the interfoliate space. This
229 observation is in accordance with previous works on the dehydration of Ca-smectite (Bala et
230 al., 2000; Morodome and Kawamura, 2009). Above 700° the intensities of the characteristic
231 peaks of dolomite decrease and new peaks attributed to calcite, periclase and lime, appear.
232 These results agree with the existing bibliography (Olszak-Humienik and Jablonski, 2015)
233 describing the thermal decomposition of dolomite as a two-stage process which proceeds as
234 follows :

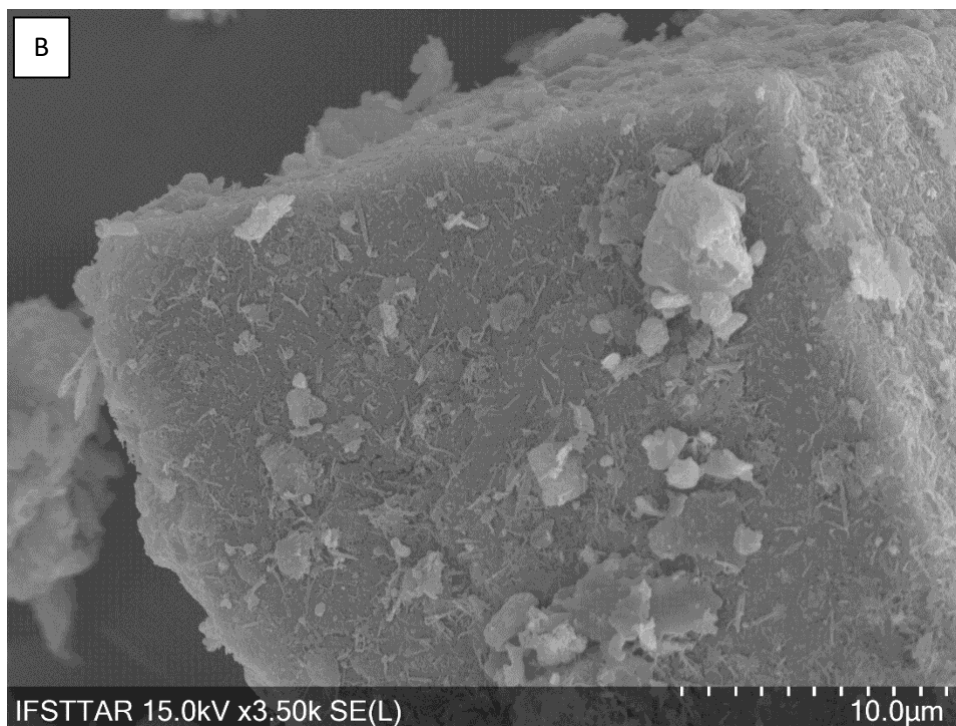


237 At 800°C all the characteristic peaks of dolomite and calcite have disappeared, demonstrating
238 its full dissociation. On the other hand, we observe the appearance of a diffraction peak at $2\theta =$
239 33° . It is attributed to belite, a dicalcium silicate common in anhydrous cement. The formation
240 of belite can be explained by a recombination phenomenon between the silicon from clayey
241 phases and the calcium from dolomite (Xie et al., 2016). However, the low crystallinity of this
242 new phase does not allow us to determine the type of polymorph. At 900°C all the peaks of
243 dehydrated Ca-smectite and biotite disappeared, reflecting a complete loss of crystallinity of
244 these two phases. This loss of crystallinity is correlated with recrystallization phenomena since
245 the formation of new crystalline phases is observed. Among them we find akermanite
246 $(\text{Ca}_2\text{MgSi}_2\text{O}_7)$, augite $((\text{Si},\text{Al})_2\text{O}_6)(\text{Ca},\text{Mg},\text{Fe},\text{Ti},\text{Al})_2$ and enstatite $(\text{Mg}_2\text{Si}_2\text{O}_6)$. Quartz and
247 hydroxylapatite $(\text{Ca}_5(\text{PO}_4)_3\text{OH})$ are not affected by the heat treatment since no relevant change
248 is observed between the raw sample and the 900°C calcined samples. Thus, the argillaceous-
249 carbonate material turned out to be sensitive to the heat treatment since loss of crystallinity of
250 the clay phases, decomposition of dolomite and recrystallization of new phases have been
251 observed.

252 Figure 5 compares SEM images of raw (Figure 5A) and the 800°C calcined (Figure 5B) sample
253 powders. Calcination at 800°C does not change the morphology of the material. Indeed, the
254 shape of the mineral particle is almost identical before and after calcination. Yet the XRD
255 analysis shows that at 800°C the dolomite has transformed into Lime and Periclase and that
256 palygorskite has lost its crystallinity. It therefore appears that the morphology of the material
257 does not reflect changes in chemistry and structure induced by calcination. A deeper
258 investigation of the changes in the structure of the clay phases as a function of the calcination
259 temperature was performed by ^{27}Al and ^{29}Si MAS NMR.



260



261

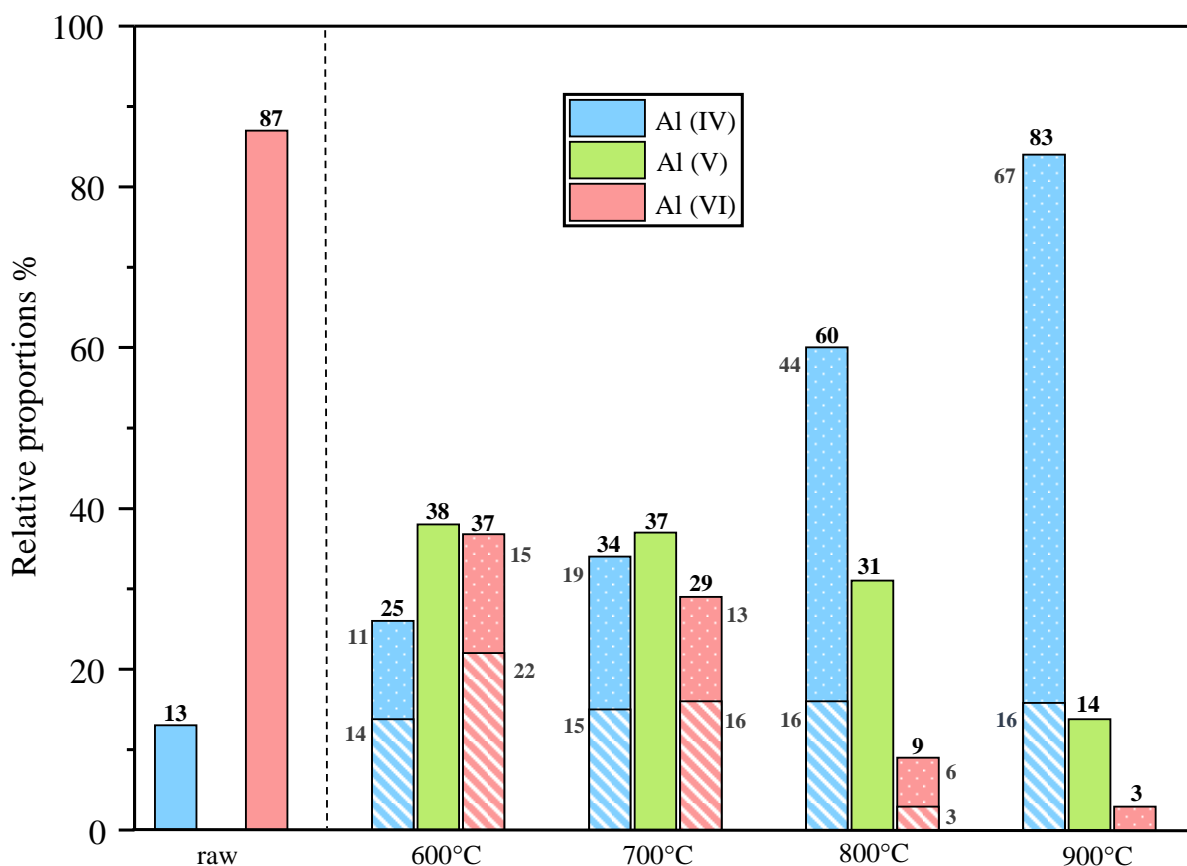
262 Figure 5: Scanning Electron Microscope images of the argillaceous-carbonate powder before
263 (A) and after calcination at 800°C (B).

264 Aluminium NMR, through the observation of the change in coordination of aluminium atoms,
265 allows us to characterize the dehydroxylation phenomenon of phyllosilicates induced by
266 calcination.

267 Figure 3 displays the evolution of the ^{27}Al MAS NMR spectra of the argillaceous-carbonate
268 samples as a function of the calcination temperature. The temperature increase leads to a
269 diminution of the intensity of the resonance associated with hexacoordinated aluminium (3
270 ppm) and the appearance of two new resonances at around 59 and 27 ppm. These two new
271 resonances can be associated with tetra and pentacoordinated aluminium, respectively (Maia et
272 al., 2014). The decrease in the proportion of 6-fold aluminium and the formation of 4 and 5-
273 fold aluminium is a consequence of the dehydroxylation resulting from the calcination of the
274 sample. The temperature increase leads to the release of hydroxyl groups linked to the clay
275 octahedra, resulting in a decrease of the coordination number of the aluminium atoms.

276 Figure 6 gives the relative proportions of the 6-, 5- and 4-fold aluminium atoms having been
277 quantified by spectral integration of the ^{27}Al NMR spectra (details in Supporting Information).
278 At 600°C a significant dehydroxylation of the argillaceous phases is observed since Al (VI)
279 evolves from 87% to 36%. By using the Rietveld quantification of the crystal phases and their
280 ideal theoretical chemical compositions we can calculate the contribution of each phase to the
281 total amount of aluminium in the sample: 62% of the total aluminium comes from Ca-smectite,
282 34% from palygorskite and 4% from biotite. It becomes clear that this decrease of more than
283 half in the proportion of Al (VI) cannot be due to the dehydroxylation of palygorskite only. So
284 it seems that Ca-smectite start to dehydroxylate at 600°C, without fully losing its crystallinity
285 since its signal remains detectable by XRD up to 800°C. These results are in agreement with
286 the observations made by Fernandez et al. (2011) who suggested that the small amount of
287 hydroxyl groups present in the smectite structure could explain the small effect of
288 dehydroxylation on its cristallinity. On the other hand, as observed in Figure 1, there is a
289 disappearance of the characteristic peaks of palygorskite from 600°C onwards. This strongest
290 thermal reactivity of palygorskite compared to Ca-smectite could be explained by its particular
291 TOT structure.

292 The hatched part of the total 6-fold aluminium in Figure 6 corresponds to the component (see
293 Supporting Information) close to the signature of the aluminium present in palygorskite and
294 smectite octahedra. It can be explained by octahedral sheets that resisted calcination. On the
295 other hand, the dotted part corresponds to the component associated with very distorted
296 octahedra. It can be seen that their relative proportions do not vary in the same way with
297 increasing temperature, specifically, the proportion of 6-fold aluminium belonging to distorted
298 sheets decreases less rapidly with increasing temperature. It can be hypothesized that the
299 passage of 6-fold to 5-fold aluminium is made through this intermediate state corresponding to
300 distorted octahedral sheets.



301

302 Figure 6: Relative proportions of the 6-, 5- and 4-fold aluminium atoms as a function of the
 303 calcination temperature.

304 From 600°C onwards 4-fold aluminium is formed (from 13 to 26 %). As for 6-fold aluminium,
 305 the 4-fold aluminium resonance is described by two components represented by hatched and
 306 dotted parts in Figure 6. The isotropic chemical shift of the “hatched” component of the 4-fold
 307 aluminium is 69 ppm (see supporting information) and could be associated with 4-fold
 308 aluminium in q3 configuration (Pardal et al., 2012). In contrast, the much lower isotropic
 309 chemical shift of the “dotted” component at 61 ppm can be associated with 4-fold aluminium
 310 in q4 configuration (Muller et al., 1986).

311 The “hatched” component appears as soon as the calcination temperature reaches 600°C and
 312 remains stable (around 15%) in spite of the temperature increase. Knowing that palygorskite
 313 becomes amorphous at 600°C (see Figure 1), we can associate this “hatched” component of 4-

314 fold aluminium with the dehydroxylation of palygorskite. Thereafter, only the "dotted"
315 component of 4-fold aluminium increases with the increase of the calcination temperature, it
316 would seem that this 4-fold aluminium is associated with the dehydroxylation of Ca-smectite
317 and biotite.

318 Concerning the 5-fold aluminium, the highest proportion is reached from 600°C, and then
319 decreases with increasing temperature. Up to 800°C its proportion remains stable because the
320 dehydroxylation of 6-fold aluminium compensates for the transformation of 5-fold aluminium
321 into 4-fold aluminium. Fernandez et al. (2011) associated the pozzolanic activity of a calcined
322 clay with the appearance of penta-coordinated aluminum within the structure of the clay.
323 Indeed, penta-coordinated aluminum turns out to be the most unstable form and the most prone
324 to react. However, it is important to remember that 4-fold aluminium is also reactive and could
325 play an important role in the pozzolanic reaction.

326 Therefore, 800°C seems to be a good calcination temperature since it allows an almost total
327 dehydroxylation of the clay phases (only 9% of 6-fold aluminium remains) while keeping a
328 large proportion of 5-fold aluminium (31%).

329 Table 2 displays the result of the Rietveld refinement of the 800°C calcined argillaceous-
330 carbonate. An amorphous phase is present and accounts for almost 28% of the total sample
331 mass. This high proportion of amorphous is mainly due to the amorphisation of palygorskite as
332 its signal is no longer observable at 800°C (Figure 1). The formation of hematite at 800°C
333 shows that part of the dolomite ($\text{CaMg}(\text{CO}_3)_2$) is actually ankerite ($\text{Ca}(\text{Fe},\text{Mg})(\text{CO}_3)_2$).
334 However, the proportion of ankerite is very low in regards to the proportion of hematite formed
335 (1.45 wt.%), which confirms the low iron value in chemical analysis results (Table 1).

336 Figure 4 displays the evolution of the ^{29}Si MAS NMR spectra of the argillaceous-carbonate
337 sample as function of the calcination temperature. From 600°C, we can observe a broadening

338 of the resonances characteristic of the Q3 of the clayey phases. This broadening of the lines
339 reflects distribution of the silicon atoms environments and so indicates the increase in disorder
340 within the clay phases. The characteristic resonances of palygorskite are now almost
341 indistinguishable, which confirms the observations made by XRD and suggests that the
342 disappearance of its XRD peaks is not only due to its loss of crystallinity but also to strong
343 distortions within its structure.

344 At 700°C the broadening of the Q3 resonances continues, which shows that the loss of
345 crystallinity of the clayey phases continues. The main information is the appearance of a new
346 resonance at -71 ppm which is not common in the MAS NMR analysis of a calcined clay.
347 Skibsted (Skibsted et al., 1995) associates it with the presence of monomeric Q0 orthosilicates
348 typical of belite (C₂S) one of the anhydrous phases of the clinker. That confirms the
349 observations made by XRD and the possible reaction between silicon from clayey phases and
350 calcium from dolomite. The trend will continue at 800°C with a widening of the Q3 resonances
351 and an increase in the proportion of Q0 associated with belite. There is also the appearance of
352 a new resonance at -74 ppm which can be associated with silicon in Q1 configuration (Janes
353 and Oldfield, 1985) which is attributed to akermanite detected by XRD. By crossing these
354 results with XRD, we can highlight that recrystallization phenomena begin as early as 800°C,
355 but the low crystallinity of these new phases prevents their characterization by XRD at this
356 temperature.

357 Between 800 and 900°C the width of Q0 resonance of belite decreases whereas its intensity
358 increases. This means that the proportion and the level of crystallinity of the neo-formed belite
359 are increasing. The Q1 resonance of akermanite is also more intense. The characteristic Q2
360 resonances of the augite (-72 ppm) and the enstatite (-84 ppm) cannot be observed because they
361 overlap with the broader resonances from the calcined clay (MacKenzie and Meinhold, 1994;
362 Huang et al., 2012).

363 It is important to specify that the chosen repetition time does not allow to be quantitative for
364 quartz. Indeed, after several tests it seems that it is necessary to use a T_1 close to 3600 seconds
365 to allow a complete relaxation, which complicates quantification. We have then calculated the
366 proportion of belite formed at 800°C from the results of chemical analysis (XRF), quantification
367 of crystal phases (XRD) and ^{29}Si MAS NMR. In order to carry out this calculation we made the
368 hypothesis that Quartz does not react. Knowing the total amount of silicon (from XRF results)
369 and the wt.% proportion of quartz (from XRD Rietveld refinement) in the raw sample we re-
370 calculated the total amount of silicon present in the system without quartz. Then, by using the
371 ^{29}Si MAS NMR spectrum of calcined sample, we quantified the relative repartition of silicon
372 belonging to the belite and to the rest of the system (without quartz) at 800°C and we calculated
373 their respective molar proportions. Subsequently, neglecting the minor phases, we used
374 theoretical ideal formulas for palygorskite, smectite, and belite to convert molar proportions of
375 silicon to weight proportions of phases. Calculations give a proportion of ~8 wt.% of belite in
376 the sample calcined at 800°C. If we compare this value with the amount of crystalline belite
377 obtained by Rietveld refining (~4,5 wt.%), it appears that the low crystallinity of belite causes
378 the XRD to underestimate it by half.

379 The formation of belite during the calcination of a mixture of palygorskite and dolomite has
380 already been observed (Xie et al., 2016). belite represents on average 15 to 20% of the total
381 cement phases and is responsible of the long-term mechanical properties (Bouzidi et al., 2014).
382 Its presence in the sample calcined at 800°C is therefore good news, assuming that it is reactive.
383 However, the formation of lime and periclase could be troublesome for further use in cement
384 systems (carbonation and post-hardening swelling).

385

386

387 5. CONCLUSION

388 The study of the thermal reactivity of this argillaceous carbonate highlighted its potential for a
389 use as a SCM. Indeed, the palygorskite which composes this sample seems to be very sensitive
390 to heat treatment and it dehydroxylated very easily from 600°C, certainly because of its so
391 particular structure. Moreover, the calcination of the clay mixed with carbonate allowed to
392 highlight the formation of belite (C₂S) from 700°C. The chemistry of the system favours the
393 reaction of calcium from dolomite and silicon from clayey phases to form this cementitious
394 phase. The calcined palygorskite associated with belite formation make this carbonate-material
395 a very interesting system for use as a cementitious addition because of its double reactivity
396 (pozzolanic and hydraulic). For the rest, it would be interesting to study the influence of the
397 clay phase/carbonate ratio on the quality and quantity of neoformed belite and finally to test the
398 reactivity of this sample.

399 ACKNOWLEDGMENTS

400 Dr. Bruno Lanson and Nathaniel Findling are thanked for their valuable help with the use of
401 Profex software for Rietveld refinement.

402 References

- 403 Bala, P., Samantaray, B.K., Srivastava, S.K., 2000. Dehydration transformation in Ca-
404 montmorillonite. *Bull. Mater. Sci.* 23, 61–67. <https://doi.org/10.1007/BF02708614>
405 Barron, P.F., Frost, R.L., Qlil, N., 1985. Solid state ²⁹Si NMR examination of the 2:1 ribbon
406 magnesium silicates, sepiolite and palygorskite. *Am. Mineral.* 70, 758–766.
407 Blanco, C., González, F., Pesquera, C., Benito, I., Mendioroz, S., Pajares, J.A., 1989.
408 Differences Between One Aluminic Palygorskite and Another Magnesic by Infrared
409 Spectroscopy. *Spectrosc. Lett.* 22, 659–673.
410 <https://doi.org/10.1080/00387018908053926>
411 Bonavetti, V.L., Rahhal, V.F., Irassar, E.F., 2001. Studies on the carboaluminate formation in
412 limestone filler-blended cements. *Cem. Concr. Res.* 31, 853–859.
413 [https://doi.org/10.1016/S0008-8846\(01\)00491-4](https://doi.org/10.1016/S0008-8846(01)00491-4)
414 Boudriche, L., Calvet, R., Hamdi, B., Balard, H., 2011. Effect of acid treatment on surface
415 properties evolution of attapulgite clay: An application of inverse gas chromatography.
416 *Colloids Surf. Physicochem. Eng. Asp.* 392, 45–54.
417 <https://doi.org/10.1016/j.colsurfa.2011.09.031>

418 Bouzidi, M.A., Tahakourt, A., Bouzidi, N., Merabet, D., 2014. Synthesis and Characterization
419 of belite Cement with High Hydraulic Reactivity and Low Environmental Impact.
420 Arab. J. Sci. Eng. 39, 8659–8668. <https://doi.org/10.1007/s13369-014-1471-2>

421 Brown, I.W.M., MacKenzie, K.J.D., Meinhold, R.H., 1987. The thermal reactions of
422 montmorillonite studied by high-resolution solid-state ²⁹Si and ²⁷Al NMR 3265–
423 3275.

424 Cancio Díaz, Y., Sánchez Berriel, S., Heierli, U., Favier, A.R., Sánchez Machado, I.R.,
425 Scrivener, K.L., Martirena Hernández, J.F., Habert, G., 2017. Limestone calcined clay
426 cement as a low-carbon solution to meet expanding cement demand in emerging
427 economies. Dev. Eng. 2, 82–91. <https://doi.org/10.1016/j.deveng.2017.06.001>

428 Danner, T., Norden, G., Justnes, H., 2018a. Characterisation of calcined raw clays suitable as
429 supplementary cementitious materials. Appl. Clay Sci. 162, 391–402.
430 <https://doi.org/10.1016/j.clay.2018.06.030>

431 Danner, T., Norden, G., Justnes, H., 2018b. Characterisation of calcined raw clays suitable as
432 supplementary cementitious materials. Appl. Clay Sci. 162, 391–402.
433 <https://doi.org/10.1016/j.clay.2018.06.030>

434 Doebelin, N., Kleeberg, R., 2015. *Profex*: a graphical user interface for the Rietveld
435 refinement program *BGMN*. J. Appl. Crystallogr. 48, 1573–1580.
436 <https://doi.org/10.1107/S1600576715014685>

437 El-Diadamony, H., Amer, A.A., Sokkary, T.M., El-Hoseny, S., 2018. Hydration and
438 characteristics of metakaolin pozzolanic cement pastes. HBRC J. 14, 150–158.
439 <https://doi.org/10.1016/j.hbrj.2015.05.005>

440 Escalante, J.I., Gómez, L.Y., Johal, K.K., Mendoza, G., Mancha, H., Méndez, J., 2001.
441 Reactivity of blast-furnace slag in Portland cement blends hydrated under different
442 conditions. Cem. Concr. Res. 31, 1403–1409. [https://doi.org/10.1016/S0008-8846\(01\)00587-7](https://doi.org/10.1016/S0008-8846(01)00587-7)

444 Fernandez, R., Martirena, F., Scrivener, K.L., 2011. The origin of the pozzolanic activity of
445 calcined clay minerals: A comparison between kaolinite, illite and montmorillonite.
446 Cem. Concr. Res. 41, 113–122. <https://doi.org/10.1016/j.cemconres.2010.09.013>

447 Frydman, L., Harwood, J.S., 1995. Isotropic Spectra of Half-Integer Quadrupolar Spins from
448 Bidimensional Magic-Angle Spinning NMR 5367–5368.

449 Galan, E., 1996. Properties and applications of palygorskite-sepiolite clays. Clay Miner. 31,
450 443–453. <https://doi.org/10.1180/claymin.1996.031.4.01>

451 Garg, N., Skibsted, J., 2016. Pozzolanic reactivity of a calcined interstratified illite/smectite
452 (70/30) clay. Cem. Concr. Res. 79, 101–111.
453 <https://doi.org/10.1016/j.cemconres.2015.08.006>

454 Garg, N., Skibsted, J., 2014. Thermal Activation of a Pure Montmorillonite Clay and Its
455 Reactivity in Cementitious Systems. J. Phys. Chem. C 118, 11464–11477.
456 <https://doi.org/10.1021/jp502529d>

457 Hollanders, S., Adriaens, R., Skibsted, J., Cizer, Ö., Elsen, J., 2016. Pozzolanic reactivity of
458 pure calcined clays. Appl. Clay Sci. 132–133, 552–560.
459 <https://doi.org/10.1016/j.clay.2016.08.003>

460 Horpibulsuk, S., Phojan, W., Suddepong, A., Chinkulkijniwat, A., Liu, M.D., 2012. Strength
461 development in blended cement admixed saline clay. Appl. Clay Sci. 55, 44–52.
462 <https://doi.org/10.1016/j.clay.2011.10.003>

463 Huang, X., Ni, W., Cui, W., Wang, Z., Zhu, L., 2012. Preparation of autoclaved aerated
464 concrete using copper tailings and blast furnace slag. Constr. Build. Mater. 27, 1–5.
465 <https://doi.org/10.1016/j.conbuildmat.2011.08.034>

466 Huntzinger, D.N., Eatmon, T.D., 2009. A life-cycle assessment of Portland cement
467 manufacturing: comparing the traditional process with alternative technologies. *J.*
468 *Clean. Prod.* 17, 668–675. <https://doi.org/10.1016/j.jclepro.2008.04.007>

469 Ipavec, A., Gabrovšek, R., Vuk, T., Kaučič, V., Maček, J., Meden, A., 2011. Carboaluminate
470 Phases Formation During the Hydration of Calcite-Containing Portland Cement:
471 Carboaluminate Phase Formation. *J. Am. Ceram. Soc.* 94, 1238–1242.
472 <https://doi.org/10.1111/j.1551-2916.2010.04201.x>

473 Janes, N., Oldfield, E., 1985. Prediction of silicon-29 nuclear magnetic resonance chemical
474 shifts using a group electronegativity approach: applications to silicate and
475 aluminosilicate structures. *J. Am. Chem. Soc.* 107, 6769–6775.
476 <https://doi.org/10.1021/ja00310a004>

477 Krishnan, S., Emmanuel, A.C., Shah, V., Parashar, A., Mishra, G., Maity, S., Bishnoi, S.,
478 2019. Industrial production of limestone calcined clay cement: experience and
479 insights. *Green Mater.* 7, 15–27. <https://doi.org/10.1680/jgrma.18.00003>

480 Lippmaa, E., Maegi, M., Samoson, A., Engelhardt, G., Grimmer, A.R., 1980. Structural
481 studies of silicates by solid-state high-resolution silicon-29 NMR. *J. Am. Chem. Soc.*
482 102, 4889–4893. <https://doi.org/10.1021/ja00535a008>

483 Mackenzie, K.J.D., Brown, I.W.M., Cardile, C.M., Meinhold, R.H., 1987. The thermal
484 reactions of muscovite studied by high-resolution solid-state 29-Si and 27-Al NMR. *J.*
485 *Mater. Sci.* 22, 2645–2654. <https://doi.org/10.1007/BF01082158>

486 MacKenzie, K.J.D., Meinhold, R.H., 1994. The thermal reactions of talc studied by 29Si and
487 25Mg MAS NMR. *Thermochim. Acta* 244, 195–203. [https://doi.org/10.1016/0040-](https://doi.org/10.1016/0040-6031(94)80219-X)
488 [6031\(94\)80219-X](https://doi.org/10.1016/0040-6031(94)80219-X)

489 Maia, A.Á.B., Angélica, R.S., de Freitas Neves, R., Pöllmann, H., Straub, C., Saalwächter, K.,
490 2014. Use of 29Si and 27Al MAS NMR to study thermal activation of kaolinites from
491 Brazilian Amazon kaolin wastes. *Appl. Clay Sci.* 87, 189–196.
492 <https://doi.org/10.1016/j.clay.2013.10.028>

493 Massiot, D., Fayon, F., Capron, M., King, I., Le Calvé, S., Alonso, B., Durand, J.-O., Bujoli,
494 B., Gan, Z., Hoatson, G., 2002. Modelling one- and two-dimensional solid-state NMR
495 spectra: Modelling 1D and 2D solid-state NMR spectra. *Magn. Reson. Chem.* 40, 70–
496 76. <https://doi.org/10.1002/mrc.984>

497 Morodome, S., Kawamura, K., 2009. Swelling Behavior of Na- and Ca-Montmorillonite up to
498 150°C by in situ X-ray Diffraction Experiments. *Clays Clay Miner.* 57, 150–160.
499 <https://doi.org/10.1346/CCMN.2009.0570202>

500 Muller, D., Gessner, W., Samoson, A., Lippmaa, E., 1986. Solid-state Aluminium-27 Nuclear
501 Magnetic Resonance Chemical Shift and Quadrupole Coupling Data for Condensed
502 AlO₄ Tetrahedra. *J Chem Soc Dalton Trans* 5.

503 Olszak-Humienik, M., Jablonski, M., 2015. Thermal behavior of natural dolomite. *J. Therm.*
504 *Anal. Calorim.* 119, 2239–2248. <https://doi.org/10.1007/s10973-014-4301-6>

505 Pardal, X., Brunet, F., Charpentier, T., Pochard, I., Nonat, A., 2012. 27Al and 29Si Solid-
506 State NMR Characterization of Calcium-Aluminosilicate-Hydrate. *Inorg. Chem.* 51,
507 1827–1836. <https://doi.org/10.1021/ic202124x>

508 Prasad, M.S., Reid, K.J., Murray, H.H., 1991. Kaolin: processing, properties and applications.
509 *Appl. Clay Sci.* 6, 87–119. [https://doi.org/10.1016/0169-1317\(91\)90001-P](https://doi.org/10.1016/0169-1317(91)90001-P)

510 Sakai, E., Miyahara, S., Ohsawa, S., Lee, S.-H., Daimon, M., 2005. Hydration of fly ash
511 cement. *Cem. Concr. Res.* 35, 1135–1140.
512 <https://doi.org/10.1016/j.cemconres.2004.09.008>

513 Sanz, J., Serratos, J.M., 1984. Silicon-29 and aluminum-27 high-resolution MAS-NMR
514 spectra of phyllosilicates. *J. Am. Chem. Soc.* 106, 4790–4793.
515 <https://doi.org/10.1021/ja00329a024>

516 Scrivener, K., Martirena, F., Bishnoi, S., Maity, S., 2018. Calcined clay limestone cements
517 (LC3). *Cem. Concr. Res.* 114, 49–56. <https://doi.org/10.1016/j.cemconres.2017.08.017>
518 Skibsted, J., Jakobsen, H.J., Hall, C., 1995. Quantification of calcium silicate phases in
519 Portland cements by ²⁹Si MAS NMR spectroscopy. *J. Chem. Soc. Faraday Trans.* 91,
520 4423. <https://doi.org/10.1039/ft9959104423>
521 Soltani, A., Tarighat, A., Varmazyari, M., 2018. Calcined Marl and Condensed Silica Fume as
522 Partial Replacement for Ordinary Portland Cement. *Int. J. Civ. Eng.* 16, 1549–1559.
523 <https://doi.org/10.1007/s40999-018-0289-9>
524 Trümer, A., Ludwig, H.-M., Schellhorn, M., Diedel, R., 2019. Effect of a calcined
525 Westerwald bentonite as supplementary cementitious material on the long-term
526 performance of concrete. *Appl. Clay Sci.* 168, 36–42.
527 <https://doi.org/10.1016/j.clay.2018.10.015>
528 W.F.Bradley, 1940. The structural scheme of attapulgite, in: *American Mineralogist*. pp. 405–
529 410.
530 Xie, J., Chen, T., Xing, B., Liu, H., Xie, Q., Li, H., Wu, Y., 2016. The thermochemical
531 activity of dolomite occurred in dolomite–palygorskite. *Appl. Clay Sci.* 119, 42–48.
532 <https://doi.org/10.1016/j.clay.2015.07.014>
533
534

535

536 **SUPPORTING INFORMATIONS**

537 Spectral decompositions of the ^{27}Al MAS spectra were done by using the dmfit software
538 (Massiot et al., 2002). The initial fit was constructed from the spectrum of the argillaceous-
539 carbonate calcined at 600°C. The relevance of this fit is supported by ^{27}Al 3QMAS (Frydman
540 and Harwood, 1995) spectrum of the same sample. Signal from 6-fold aluminium that resisted
541 calcination are represented by a Lorentzian line (labelled L6_hatched). In order to account for
542 the asymmetry of the ^{27}Al resonances (due to the presence of Electric Field Gradient
543 distributions) in this amorphous sample, we chose the ‘Czsimple’ shape implemented in dmfit
544 with d=5 to use the Gaussian Isotropic Model. The isotropic chemical shift distribution is
545 described by an independent Gaussian distribution. Thus, a ‘Czsimple’ line (labelled
546 C6_dotted) was used to complete the description of the 6-fold aluminium resonance. A single
547 ‘Czsimple’ line (labelled C5) was used for the 5-fold aluminium resonance. Finally, two
548 ‘Czsimple’ lines (labelled C4_hatched and C4_dotted) were mandatory to fully describe the 4-
549 fold aluminium resonance. Parameters for the five lines are gathered in Table 3. Except
550 amplitudes, all other parameters were kept constant when fitting the ^{27}Al MAS spectra of the
551 argillaceous-carbonate samples calcined at 700, 800 and 900°C. Table 4 gives the relative
552 proportions of the lines as a function of the calcination temperature.

553

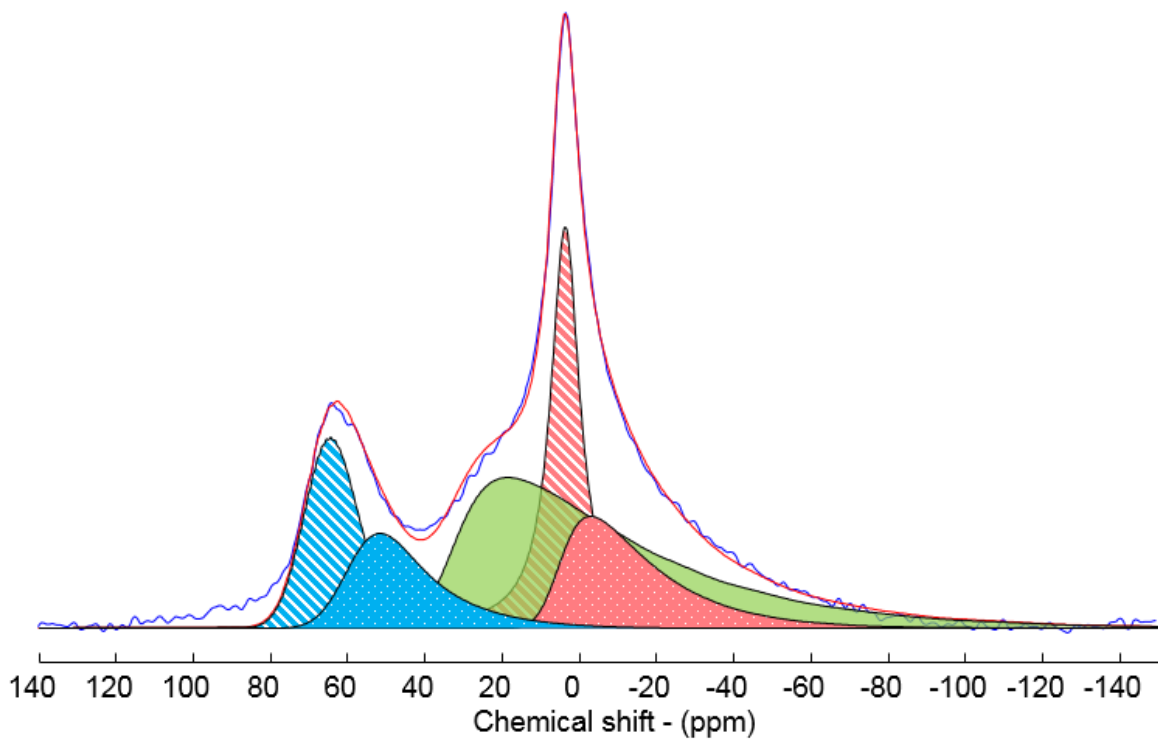
554

555

556

557

558

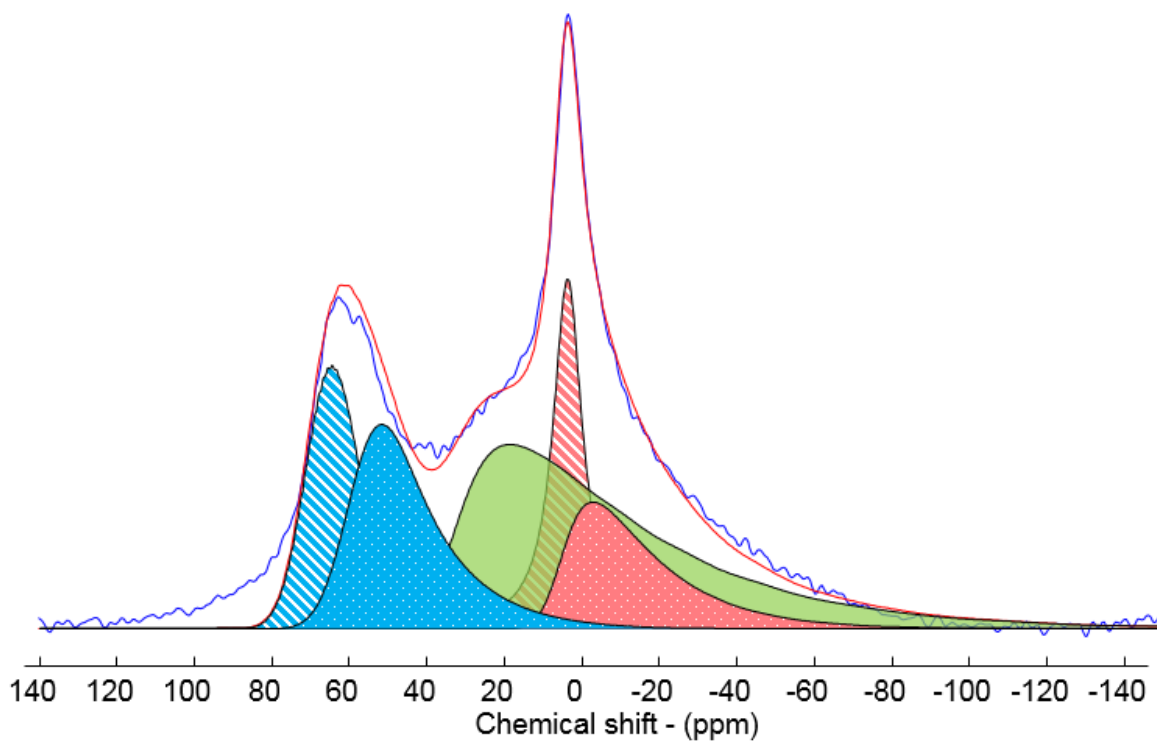


559

560 **Figure S1: Spectral integration of the ^{27}Al MAS NMR spectrum of the argillaceous-carbonate**

561

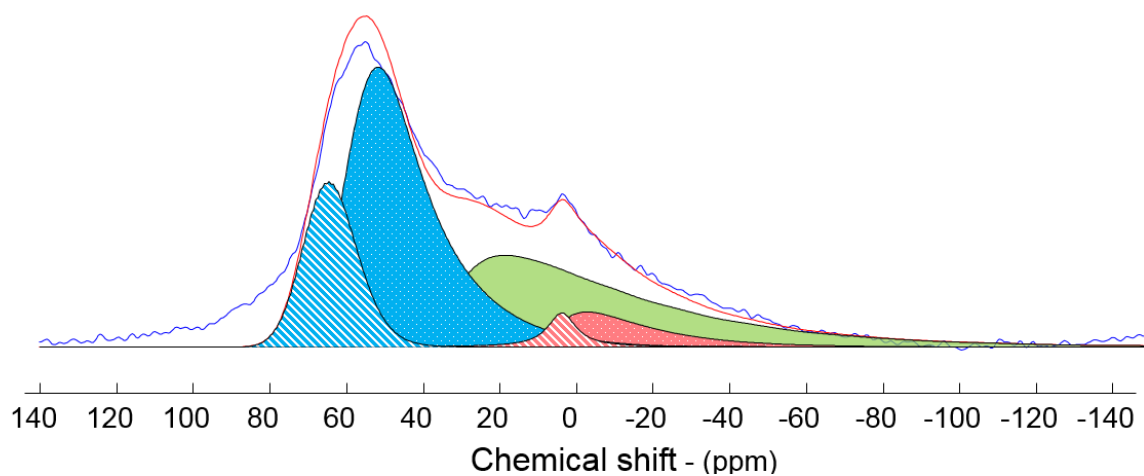
calcined at 600°C



562

563 **Figure S2: Spectral integration of the ^{27}Al MAS NMR spectrum of the argillaceous-carbonate**

564 **calcined at 700°C**

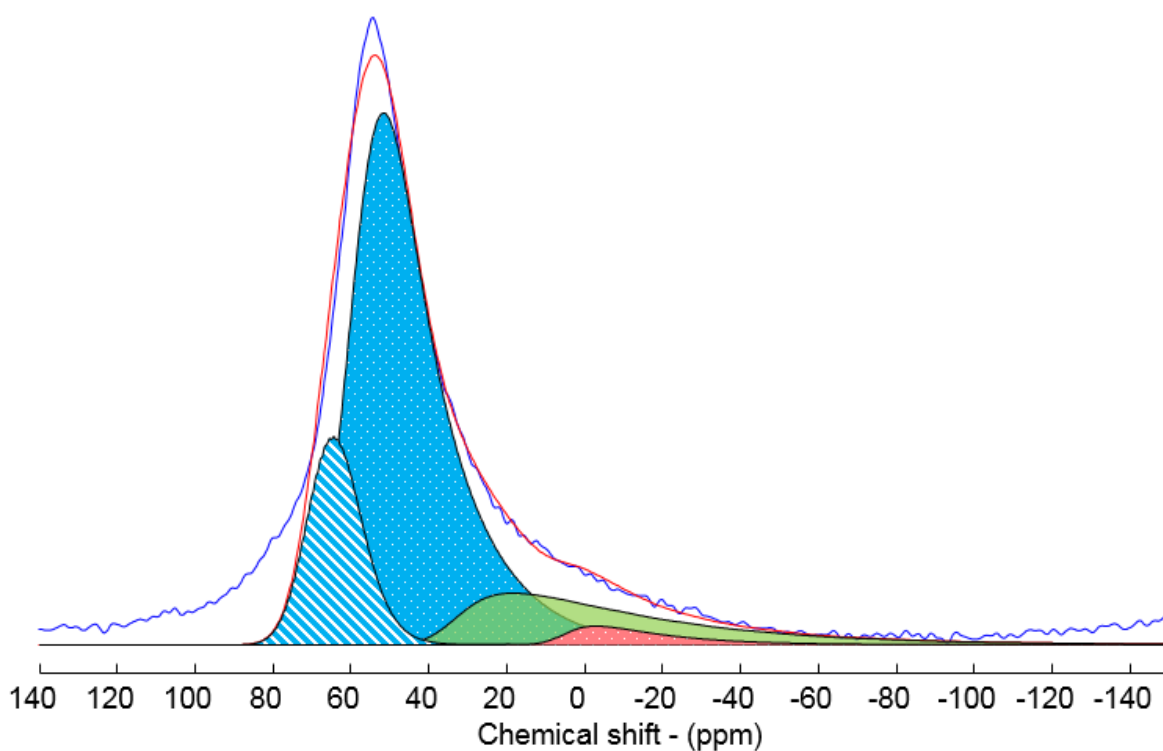


565

566 **Figure S3: Spectral integration of the ^{27}Al MAS NMR spectrum of the argillaceous-carbonate**

567 **calcined at 800°C**

568



569

570 **Figure S4: Spectral integration of the ^{27}Al MAS NMR spectrum of the argillaceous-carbonate**

571 **calcined at 900°C**

572

573 **Table S1: Parameters for the ^{27}Al MAS NMR spectral decompositions. δ_{iso} is the isotropic**
 574 **chemical shift, C_Q is the mean quadrupolar product (GIM) and FWHM CS is the full width at**
 575 **half maximum of the Gaussian distribution of isotropic chemical shift.**

Component	Shape	δ_{iso} (ppm)	Width (ppm)	C_Q (MHz)	FWHM CS (ppm)
L6_hatched	Lorentzienne	3.8	9.0		
C6_dotted	CzSimple	6.5		7.0	10.0
C5	CzSimple	35.0		10.0	14.0
C4_dotted	CzSimple	61.0		6.5	15.0
C4_hatched	CzSimple	69.0		3.5	14.0

576

577

578 **Table S2: Relative Proportions of the components of ^{27}Al MAS NMR spectra as function of the**
 579 **calcination temperature**

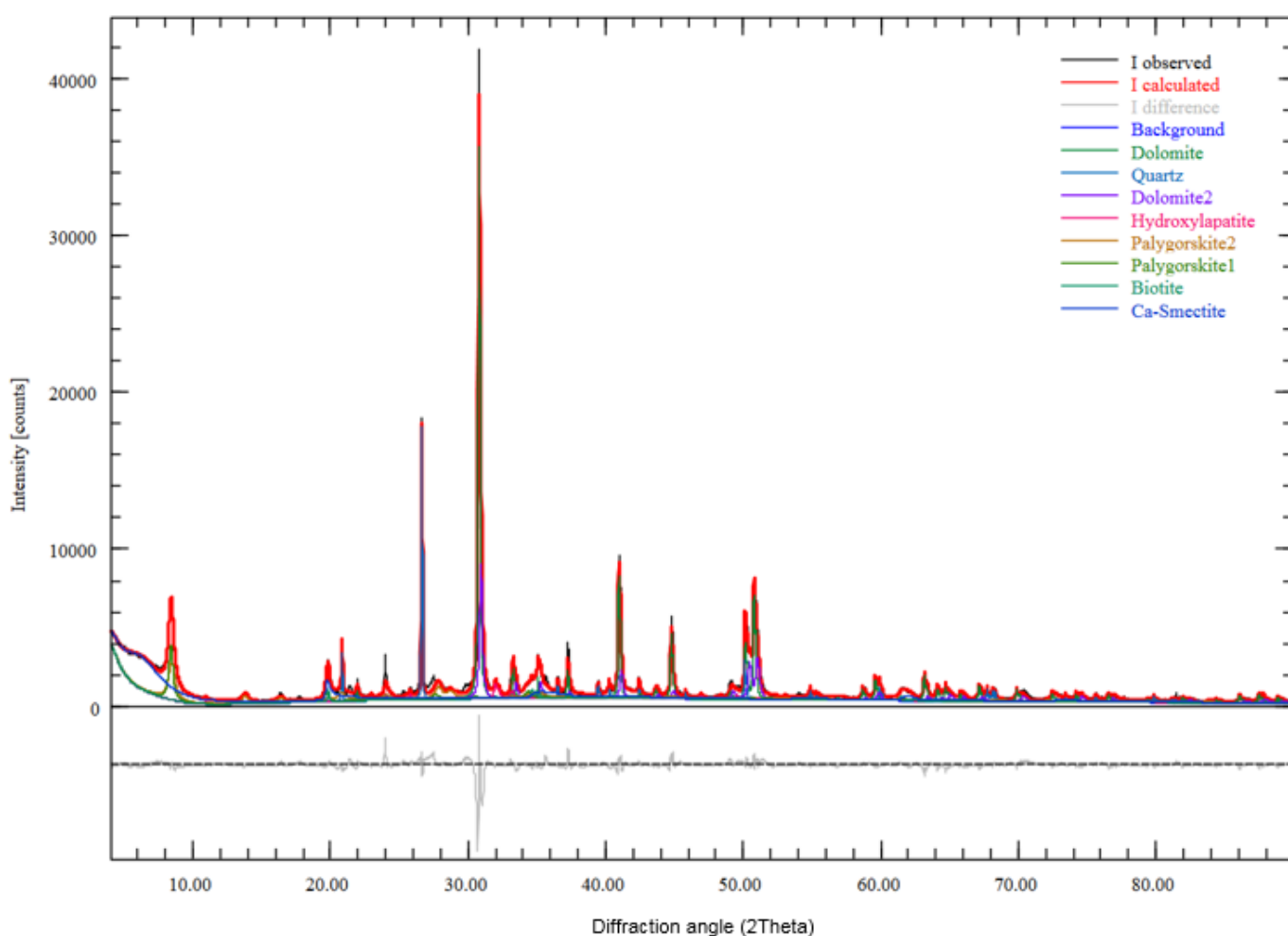
	C4_hatched	C4_dotted	C5	L6_hatched	C6_dotted
600°C	14	11	38	22	15
700°C	15	19	37	16	13
800°C	16	44	31	3	6
900°C	16	67	14	0	3

580

581

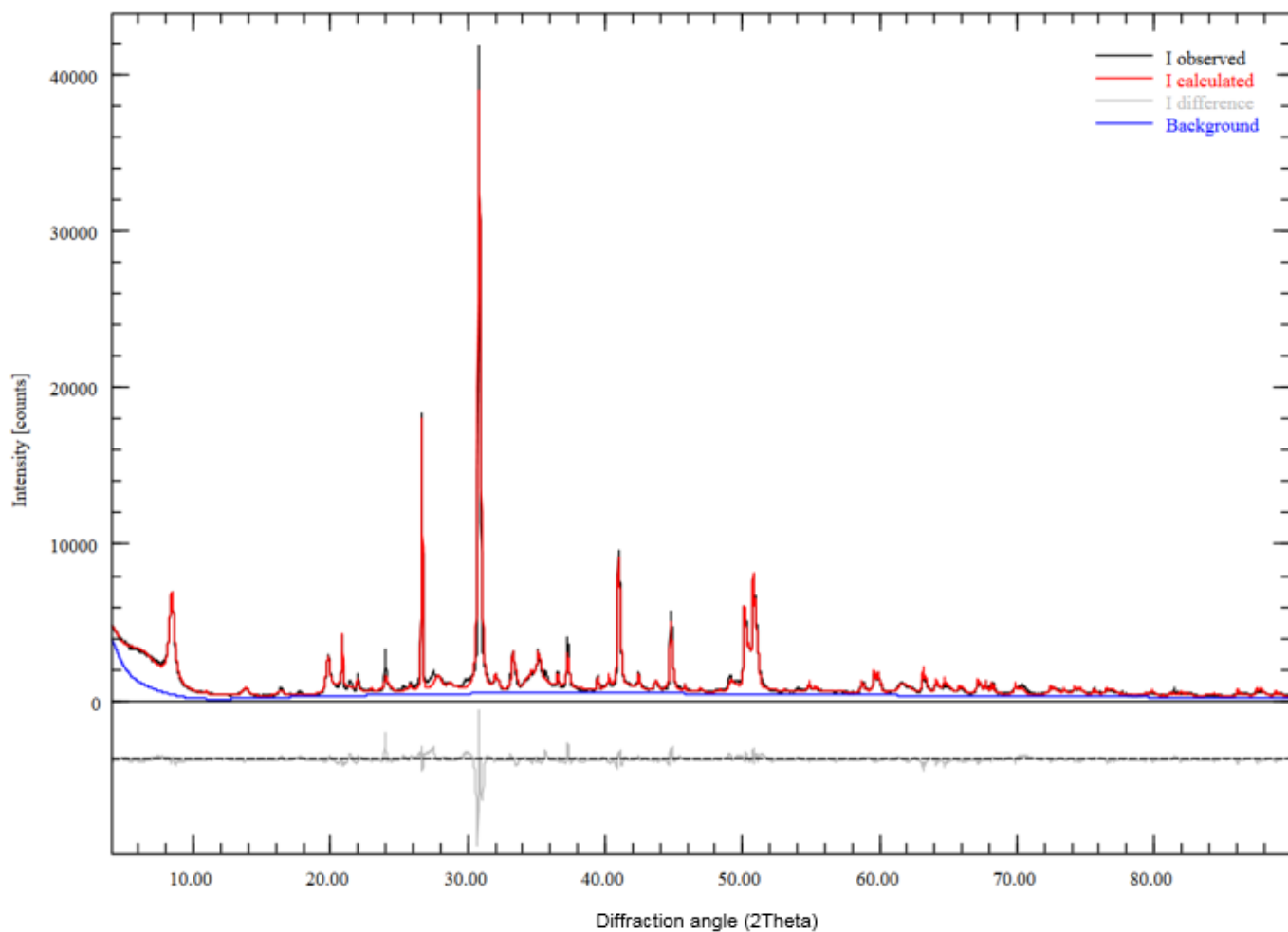
582 The Rietveld quantification of the raw and calcined material at 800°C was performed using the
 583 Profex Rietveld refinement program (Doebelin and Kleeberg, 2015). Ideal structural phases

584 have been used and refined as best as possible. The sample is a natural sample made of a mixture
585 of several phases, which explains the difficulty in obtaining a perfect fit. For the raw sample
586 two different palygorskite crystal structures (palygorskite1 and palygorskite2) and two
587 dolomite (dolomite and dolomite2) have been necessary to optimize the fit. The high R_{wp} value
588 for the refinement of the raw sample is explained by a difficulty to fit the shape of the
589 characteristic peaks of dolomite. The presence of a low proportion of ankerite may explain this
590 difficulty. Concerning the refinement of the 800°C calcined material, to simulate the dehydrated
591 smectite, crystalline structure of a zero-water layer potassium smectite was used.



592

593 **Figure S5 : Rietveld refinement of the raw argillaceous-carbonate (with peaks of phases)**



594

595 **Figure S6 : Rietveld refinement of the raw argillaceous-carbonate (without peaks of phases)**

596

597 **Table S3: Statistics of the Rietveld refinement of the raw argillaceous-carbonate**

Statistics	$R_{wp} = 10.24$	$R_{exp} = 3.14$	$\chi^2 = 10.63$	$GoF = 3.26$
-------------------	------------------	------------------	------------------	--------------

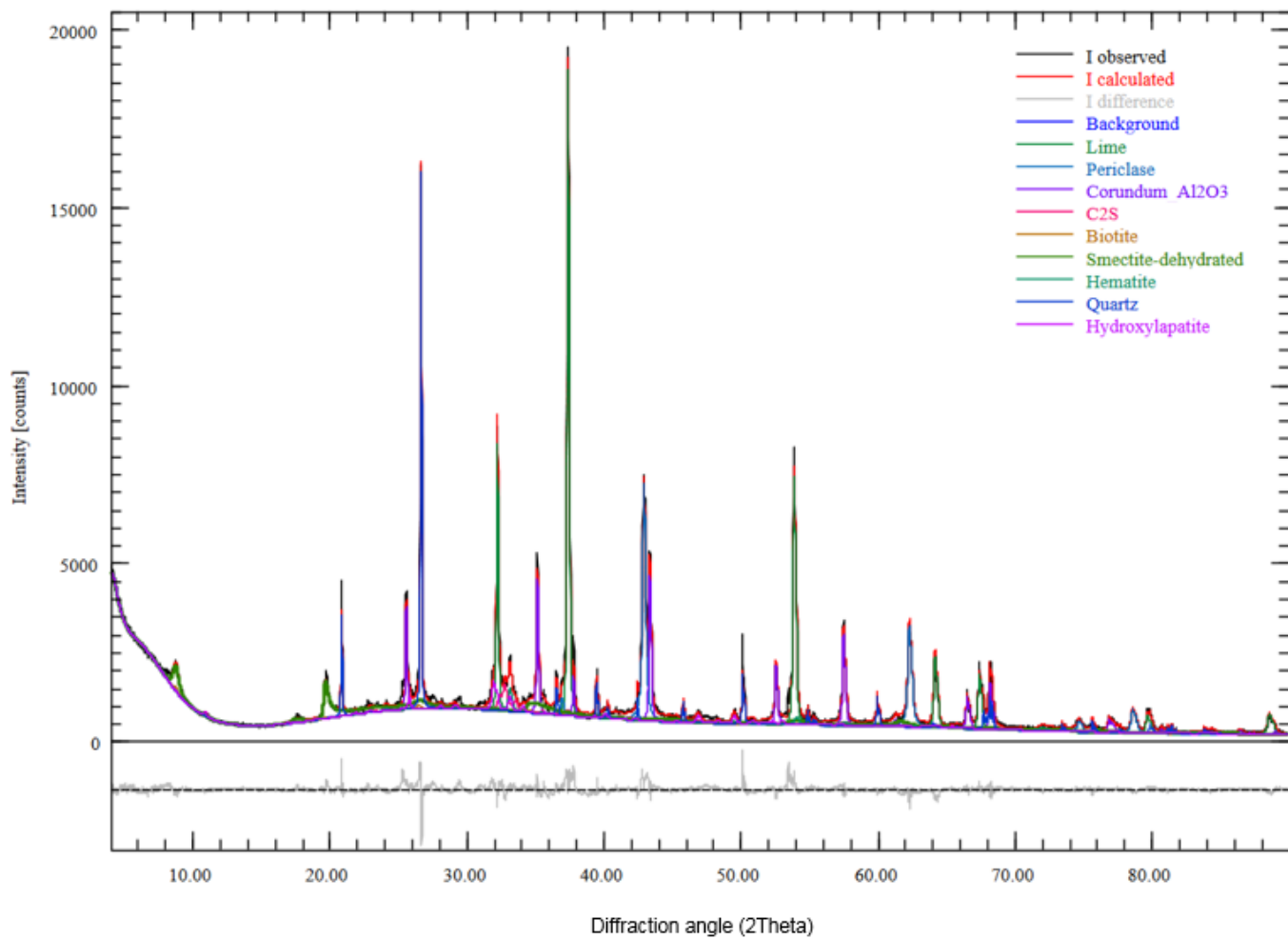
598

599

600

601

602



603

604 **Figure S7 : Rietveld refinement of the argillaceous-carbonate calcined at 800°C (with peaks of**
 605 **phases)**

606

607

608

609

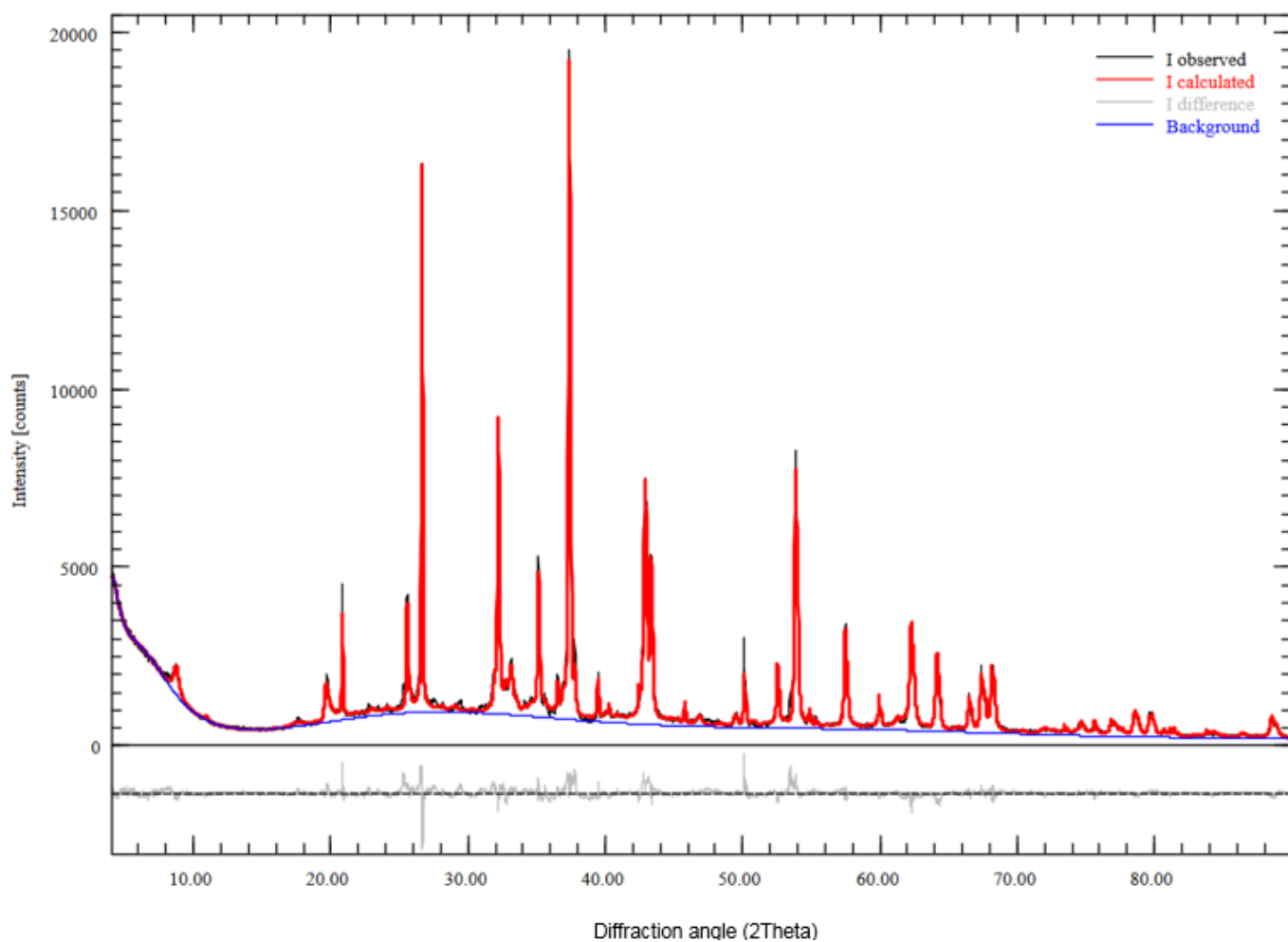
610

611

612

613

614



615

616 **Figure S8 : Rietveld refinement of the argillaceous-carbonate calcined at 800°C (without peaks**
617 **of phases)**

618

619

620 **Table S4: Statistics of the Rietveld refinement of the argillaceous-carbonate calcined at 800°C**

Statistics	$R_{wp} = 6.74$	$R_{exp} = 3.26$	$X^2 = 4.27$	$GoF = 2.07$
-------------------	-----------------	------------------	--------------	--------------

621

622 **References**

- 623 Doebelin, N., Kleeberg, R., 2015. *Profex* : a graphical user interface for the Rietveld refinement
624 program *BGMN*. *J. Appl. Crystallogr.* 48, 1573–1580.
625 <https://doi.org/10.1107/S1600576715014685>
- 626 Frydman, L., Harwood, J.S., 1995. Isotropic Spectra of Half-Integer Quadrupolar Spins from
627 Bidimensional Magic-Angle Spinning NMR 5367–5368.
- 628 Massiot, D., Fayon, F., Capron, M., King, I., Le Calvé, S., Alonso, B., Durand, J.-O., Bujoli,
629 B., Gan, Z., Hoatson, G., 2002. Modelling one- and two-dimensional solid-state NMR
630 spectra: Modelling 1D and 2D solid-state NMR spectra. *Magn. Reson. Chem.* 40, 70–
631 76. <https://doi.org/10.1002/mrc.984>
632
633